

# Polyoxomolybdate–Polypyrrole/Reduced Graphene Oxide Nanocomposite as High-Capacity Electrodes for Lithium Storage

Mi Zhang,<sup>†,⊥</sup> Tao Wei,<sup>†,‡,⊥</sup> A-Man Zhang,<sup>†</sup> Shun-Li Li,<sup>†</sup> Feng-Cui Shen,<sup>§</sup> Long-Zhang Dong,<sup>†,⊕</sup> Dong-Sheng Li,<sup>||,⊕</sup> and Ya-Qian Lan<sup>\*,†,⊕</sup>

<sup>†</sup>Jiangsu Key Laboratory of Biofunctional Materials, College of Chemistry and Materials Science, Nanjing Normal University, Nanjing 210023, P. R. China

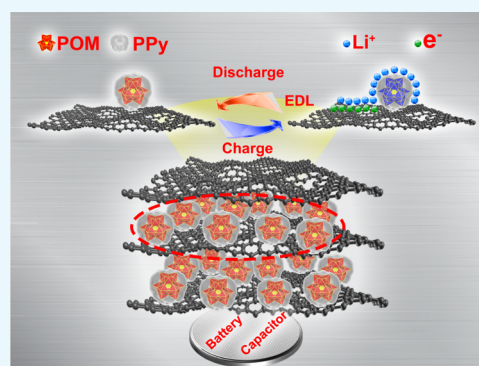
<sup>‡</sup>School of Energy and Power, Jiangsu University of Science and Technology, Zhenjiang 212003, P. R. China

<sup>§</sup>School of Biological and Chemical Engineering, Anhui Polytechnic University, Wuhu 241000, P. R. China

<sup>||</sup>College of Materials and Chemical Engineering, Key Laboratory of Inorganic Nonmetallic Crystalline and Energy Conversion Materials, China Three Gorges University, Yichang 443002, P. R. China

## S Supporting Information

**ABSTRACT:** A nanocomposite polyoxomolybdate ( $\text{PMo}_{12}$ )–polypyrrole (PPy)/reduced graphene oxide (RGO) is fabricated by using a simple one-pot hydrothermal method as an electrode material for lithium-ion batteries. This facile strategy skillfully ensures that individual polyoxometalate (POM) molecules are uniformly immobilized on the RGO surfaces because of the wrapping of polypyrrole (PPy), which avoids the desorption and dissolution of POMs during cycling. The unique architecture endows the  $\text{PMo}_{12}$ –PPy/RGO with the lithium storage behavior of a hybrid battery–supercapacitor electrode: the nanocomposite with a lithium storage capacity delivers up to  $1000 \text{ mAh g}^{-1}$  at  $100 \text{ mA g}^{-1}$  after 50 cycles. Moreover, it still demonstrates an outstanding rate capability and a long cycle life ( $372.4 \text{ mAh g}^{-1}$  at  $2 \text{ A g}^{-1}$  after 400 cycles). The reversible capacity of this nanocomposite has surpassed most pristine POMs and POMs-based electrode materials reported to date.



## 1. INTRODUCTION

With the rapid increase in the global demand for portable electronic devices, electrical vehicles, and other energy-demanding equipment, lithium-ion batteries (LIBs) and supercapacitors have shown great prospect for high-density energy storage systems.<sup>1</sup> Although great efforts have been made to the rational design of novel anode materials for rechargeable LIBs, high-power LIBs still remain a great challenge resulting from the slow processes of  $\text{Li}^+$  diffusion. In contrast, supercapacitors work through the redox reactions of the pseudocapacitive active materials or the formation of electrical double-layer capacitors, but their low-energy density hampers their application in electrochemical devices.<sup>2–4</sup> To satisfy the increasing demand for high power density and energy density, it is significant to design an electrode that combines the energy of a battery and power of a supercapacitor.

Polyoxometalates (POMs) have already demonstrated great promise for electrochemical energy storage owing to their electron storage.<sup>5</sup> Particularly, Awaga and co-workers revealed that  $[\text{PMo}_{12}\text{O}_{40}]^{3-}$  exhibited a reversible 24 electrons redox during charging/discharging between  $[\text{PMo}_{12}\text{O}_{40}]^{3-}$  and  $[\text{PMo}_{12}\text{O}_{40}]^{27-}$ .<sup>6–8</sup> However, their application in LIBs and supercapacitors is still hampered because the electronic conductivity of the POMs is poor and their anions are likely to dissolve in the electrolyte.<sup>9</sup> To overcome this obstacle,

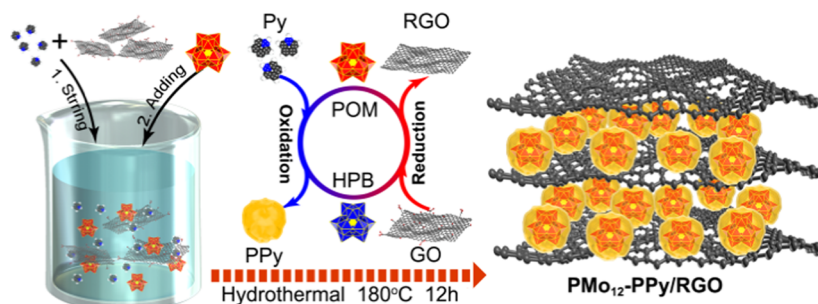
POMs are usually linked to conductive carbon substrates. For example, Song et al. reported that POMs can be anchored on single-walled carbon nanotubes (SWNTs) via  $\pi$ – $\pi$  stacking or covalent bonding, which improved the affinity of POMs to conductive network, leading to an increased lithium-ion capability.<sup>10,11</sup> Graphene oxide (GO) has attracted much interest owing to its unique properties, including chemical stability and high conductivity.<sup>12–15</sup> It is theoretically considered that graphene possesses a higher specific surface area than SWNTs.<sup>16–18</sup> However, there is still a bottleneck in the course of studies on POMs/reduced graphene oxide (RGO) nanocomposite that the low POMs loadings on graphene results in the poor performance because of the weak interaction between POMs and graphene.<sup>19</sup> Accordingly, it is still challenging to develop the appropriate linkage between POMs and graphene.

Herein, the synthesis of  $\text{H}_3\text{PMo}_{12}\text{O}_{40}$  (polyoxomolybdate ( $\text{PMo}_{12}$ ))–polypyrrole (PPy)/RGO nanocomposite (denoted as  $\text{PMo}_{12}$ –PPy/RGO) via a one-pot hydrothermal strategy is reported together with their applications for high-performance LIBs. We prepared the nanocomposite by using pyrrole (Py) to

Received: June 8, 2017

Accepted: August 28, 2017

Published: September 11, 2017

Scheme 1. Schematic Illustration of the Formation of  $\text{PMo}_{12}$ -PPy/RGO Nanocomposite

reduce  $\text{PMo}_{12}$  to obtain heteropoly blue, which was further used for the reduction of graphene accompanied by the polymerization of the Py monomer.<sup>20–23</sup> It is proved that PPy is not only an efficient reagent to improve the electron transport but also relieves the leaching of POMs into the electrolyte during cycling, leading to the enhancement of battery performance. The nanocomposite exhibits a good cycling reversibility and achieves a high capacity as a LIB anode, which can deliver a discharge capacity of  $1082.5 \text{ mAh g}^{-1}$  at  $100 \text{ mA g}^{-1}$  after 50 cycles as well as an impressive rate capability. Such an outstanding property of the nanocomposite is ascribed to the hybrid performances, which include both capacitive and battery behavior. Therefore, the synthesis of the  $\text{PMo}_{12}$ -PPy/RGO paves the way for POMs as anode materials in LIBs.

## 2. RESULTS AND DISCUSSION

**2.1. Preparation and Characterization of  $\text{PMo}_{12}$ -PPy/RGO Nanocomposite.** Scheme 1 illustrates the formation of  $\text{PMo}_{12}$ -PPy/RGO nanocomposite. We obtained  $\text{PMo}_{12}$ -PPy/RGO nanocomposite using a one-pot hydrothermal strategy by mixing  $\text{PMo}_{12}$ , Py, and GO.  $\text{PMo}_{12}$  serves as a strong oxidant, leading to the polymerization of Py, whereas  $\text{PMo}_{12}$  changes to heteropoly blue, which is used to reduce GO to RGO. The  $\text{PMo}_{12}$ -PPy nanoparticles are well distributed on the surfaces of the RGO nanosheets (NSs), which reduces the restacking of RGO to some extent together with creating a lot of mesopores to improve the accessibility of  $\text{Li}^+$  and electron.

Figure S1a shows the Raman spectrum of the as-synthesized nanocomposite. For comparison, the Raman spectra of pure RGO,  $\text{PMo}_{12}$ /RGO control samples, and  $\text{PMo}_{12}$ -PPy/RGO composite are provided. As can be observed, the pure RGO and  $\text{PMo}_{12}$ /RGO samples represent two typical Raman features at  $\sim 1351$  and  $\sim 1599 \text{ cm}^{-1}$ , corresponding to D and G bands, respectively. Compared with the D band, the intensity of the G band is apparently stronger, which indicates a higher graphitization degree of the  $\text{PMo}_{12}$ -PPy/RGO nanocomposite. In addition, a series of characteristic Raman peaks for PPy centered at about 931, 976, 1053, 1244, 1371, 1411, and  $1588 \text{ cm}^{-1}$  are observed in the  $\text{PMo}_{12}$ -PPy/RGO sample,<sup>24</sup> indicating that the polymerization of Py by  $\text{PMo}_{12}$  is conducted well and the  $\text{PMo}_{12}$ -PPy nanoparticles are distributed on the graphene sheets.<sup>25</sup> Compared with  $\text{PMo}_{12}$  and RGO, several new peaks originating from PPy are observed in the spectrum of  $\text{PMo}_{12}$ -PPy/RGO sample from the Fourier-transform infrared (FTIR) spectroscopy (Figure S1b), where the C=C and C–N stretching vibrations at  $1558$  and  $1453 \text{ cm}^{-1}$ , respectively, as well as the C–H in-plane ring-bending modes at  $1314 \text{ cm}^{-1}$  and the C–N in-plane ring deformation and bending modes at  $1182 \text{ cm}^{-1}$  can be observed.<sup>26–28</sup> In the  $\text{PMo}_{12}$ -PPy/RGO nanocomposite, the four observed charac-

teristic bands centered at  $1049$ ,  $931$ ,  $863$ , and  $790 \text{ cm}^{-1}$  are ascribed to  $\text{P–O}_v$ ,  $\text{Mo=O}_v$ ,  $\text{Mo–O}_b\text{–Mo}$ , and  $\text{Mo–O}_e\text{–Mo}$  stretching vibrations,<sup>20,29,30</sup> indicating that the  $\text{PMo}_{12}$  component has been successfully implanted into the final nanocomposite.

In contrast to  $\text{PMo}_{12}$ /RGO (Figure S2a,b), the restacking problem of the  $\text{PMo}_{12}$ -PPy/RGO nanocomposite (Figure 1a,b) is alleviated obviously and the NSs present rough surfaces

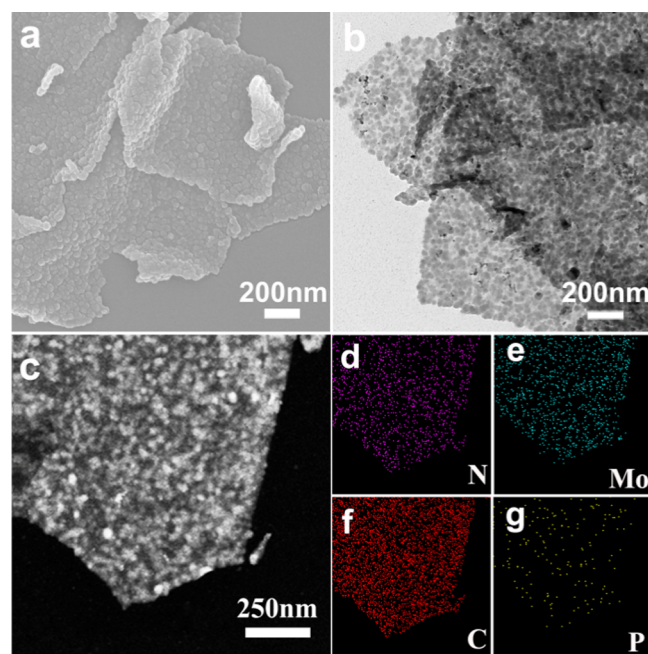


**Figure 1.** (a) SEM images of the  $\text{PMo}_{12}$ -PPy/RGO nanocomposite. (b) TEM images of the  $\text{PMo}_{12}$ -PPy/RGO nanocomposite. (c–g) Energy-dispersive spectrometry mapping of  $\text{PMo}_{12}$ -PPy/RGO.

and wrinkled edges because of the polymerization of Py homogeneously decorated with  $\text{PMo}_{12}$  on the surfaces of the RGO films.<sup>31–34</sup> The corresponding transmission electron microscopy (TEM) analysis (Figure 1b) reveals that many of  $\text{PMo}_{12}$ -PPy nanoparticles with the average size of about  $50 \text{ nm}$  homogeneously anchored on the RGO sheets. For comparison, we utilized the same strategy to prepare other nanocomposite  $\text{CoMo}_6$ -PPy/RGO based on analogous POMs ( $[\text{CoMo}_6\text{O}_{24}\text{H}_6]\cdot 7\text{H}_2\text{O}$ ). The TEM and scanning electron microscopy (SEM) images of the  $\text{CoMo}_6$ -PPy/RGO nanocomposite in Figure S2a,b reveal that  $\text{PMo}_{12}$ -PPy nanoparticles tend to be more homogeneous than  $\text{CoMo}_6$ -PPy nanoparticles on the RGO sheets. The desired spatial distribution of different elements in the  $\text{PMo}_{12}$ -PPy/RGO nanocomposite has been

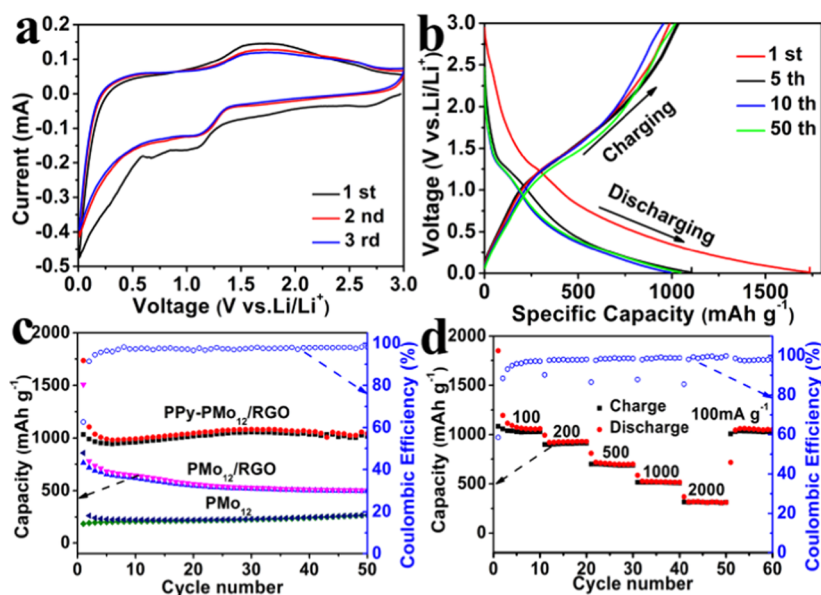


**Figure 2.** (a) Cyclic voltammetry measurements of  $\text{PMo}_{12}\text{-PPy/RGO}$  during the first three cycles at a scan rate of  $0.2 \text{ mV s}^{-1}$ . (b) Discharge–charge curves of  $\text{PMo}_{12}\text{-PPy/RGO}$  for different cycles constantly at  $100 \text{ mA g}^{-1}$ . (c) Charge/discharge capacity and Coulombic efficiency (CE) of  $\text{PMo}_{12}\text{-PPy/RGO}$ ,  $\text{PMo}_{12}\text{/RGO}$ , and  $\text{PMo}_{12}$  at  $100 \text{ mA g}^{-1}$ . (d) Rate performance of the  $\text{PMo}_{12}\text{-PPy/RGO}$  at various current densities.

examined by element mapping analysis. As shown in Figure 1c–g, P and Mo elements mainly exist in the flake-sized grains; N and C elements are uniformly distributed in the entire nanosheets. For comparison, the mappings for  $\text{PMo}_{12}\text{/RGO}$  are given in Figure S3. The corresponding mappings show that P, Mo, O elements of the  $\text{PMo}_{12}\text{-PPy/RGO}$  are more obvious than that of  $\text{PMo}_{12}\text{/RGO}$ .

The related  $\text{N}_2$  adsorption–desorption tests analyzed the pore size distribution of the obtained nanocomposite (Figure S4b). Compared with that of  $\text{PMo}_{12}\text{/RGO}$  and  $\text{CoMo}_6\text{-PPy/RGO}$  nanocomposite, the  $\text{PMo}_{12}\text{-PPy/RGO}$  nanocomposite has a rather larger and broader average pore size at around 20 nm, which is a result of the spaces between the  $\text{PMo}_{12}\text{-PPy}$  nanoparticles. The  $\text{PMo}_{12}\text{-PPy/RGO}$  nanocomposite presents the largest Brunauer–Emmett–Teller (BET) surface area ( $91.52 \text{ m}^2 \text{ g}^{-1}$ ), whereas the BET surface areas of  $\text{PMo}_{12}\text{/RGO}$  and  $\text{CoMo}_6\text{-PPy/RGO}$  are 65.5 and  $78.1 \text{ m}^2 \text{ g}^{-1}$ , respectively (Figure S4a). The larger pore size and the higher specific surface area facilitate the rapid mass transport of Li ions and electron transport, which are all correlated with the increased battery performance. The thermogravimetric analysis (TGA) results of the  $\text{PMo}_{12}\text{-PPy/RGO}$  nanocomposite and  $\text{PMo}_{12}$  are presented in Figure S5. The initial mass loss (3.6%) below  $188^\circ\text{C}$  is associated with the release of water adsorbed on the  $\text{PMo}_{12}\text{-PPy/RGO}$  nanocomposite and the further degradation of PPy, as well as the transformation from  $\text{PMo}_{12}$  to  $\text{MoO}_3$ , takes place between  $188$  and  $560^\circ\text{C}$  (Figure S5a). We can calculate from the TGA and experiment that the  $\text{PMo}_{12}\text{-PPy/RGO}$  nanocomposite possesses 72.9 wt % of  $\text{PMo}_{12}$  and 20.43 wt % of PPy.

The survey X-ray photoelectron spectroscopy (XPS) spectra of the sample before and after the cycling of LIBs demonstrate the presence of C, Mo, P, N, and O elements in the  $\text{PMo}_{12}\text{-PPy/RGO}$  nanocomposite (Figure S6). As shown in Figure S6b, the Mo 3d spectrum of  $\text{PMo}_{12}\text{-PPy/RGO}$  has two peaks at 232.3 and 235.5 eV before the electrochemical test corresponding to  $3d_{5/2}$  and  $3d_{3/2}$  of  $\text{Mo}^{6+}$ , respectively.<sup>35,36</sup> After the discharge to 0.01 V, the peaks at the binding energy of

231.9 eV are related to parts of  $\text{Mo}^{4+}$  because of the reduction of  $\text{Mo}^{6+}$  (Figure S6f).<sup>37</sup> Additionally, by deconvolution of C 1s peak (Figure S6c), the binding energy at 285 eV reveals the presence of the C–N group in the obtained nanocomposite. The corresponding fine XPS spectrum of N 1s (Figure S6d) shows that the binding energy of N 1s is about 398.3 eV, implying the existence of pyrrole N in the  $\text{PMo}_{12}\text{-PPy/RGO}$  nanocomposite. Thus, combining the fine XPS spectra for C 1s and N 1s, the existence of PPy in the obtained nanocomposite can be confirmed. From the XPS result, we can also observe the drop in the number of oxygen-containing groups, demonstrating a reduction of GO.

**2.2. Electrochemical Performances of  $\text{PMo}_{12}\text{-PPy/RGO}$  Nanocomposite.** To investigate the electrochemical activity of the  $\text{PMo}_{12}\text{-PPy/RGO}$  nanocomposite, the cyclic voltammetry (CV) measurements were tested at a constant scan rate of  $0.2 \text{ mV s}^{-1}$  (Figure 2a). The peak at about 0.6V reflects the formation of a solid electrolyte interface (SEI) film in the first cycle and then the peak disappears in the following cycles.<sup>38</sup> Although the CV curves of the first cycle are quite different in shape due to the irreversible side reactions on the electrode surfaces and interfaces, the subsequent CV curves are analogous. In the subsequent scans, broad cathodic peaks centered at about 1.2 V, as well as anodic peaks centered at around 1.6 V, are observed for the  $\text{PMo}_{12}\text{-PPy/RGO}$  electrodes, demonstrating that the reduction and oxidation of  $\text{Mo}^{39}$  (XPS results in Figure S6) is occurring during the charging/discharging processes.

The charge/discharge profiles of the  $\text{PMo}_{12}\text{-PPy/RGO}$  nanocomposites for cycle numbers 1, 2, 10, and 50 are shown in Figure 2b. In the discharge profiles, the first lithiation curve is different from the others due to the SEI formation. It is worth noting that the curves almost overlapped after the first discharge, which indicates the formation of a stable SEI film and a good electrochemical reversibility of the  $\text{PMo}_{12}\text{-PPy/RGO}$  nanocomposite. The capacity performance of the three nanocomposites is displayed in Figure 2c. The  $\text{PMo}_{12}\text{-PPy/RGO}$  nanocomposite showed a discharge  $1777.8 \text{ mAh g}^{-1}$  and

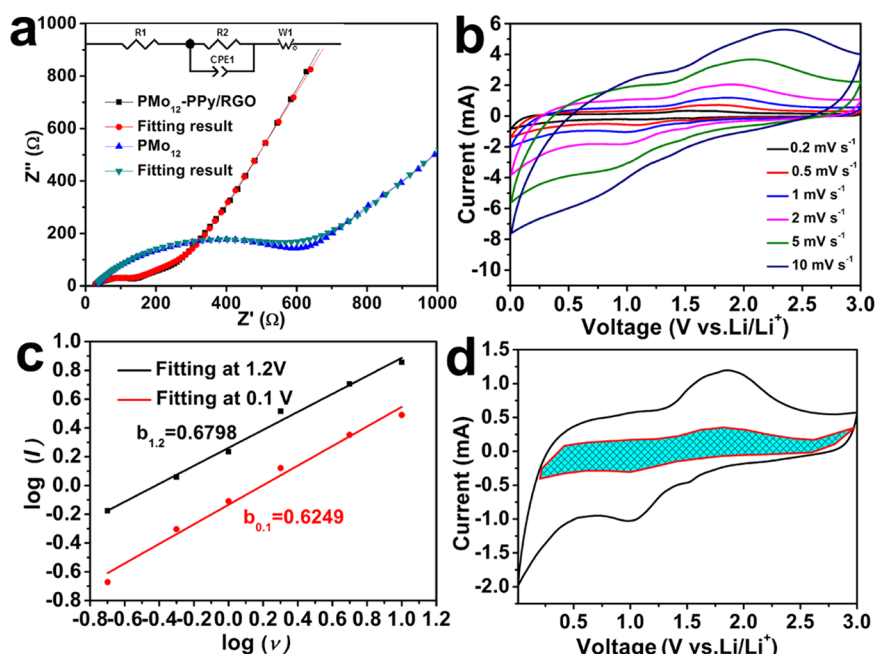


**Figure 3.** (a) Nyquist plots of  $\text{PMo}_{12}$ -PPy/RGO and microcrystal  $\text{PMo}_{12}$  electrodes after three cycles. (b) CV curves of  $\text{PMo}_{12}$ -PPy/RGO at various scan rates. (c) The  $b$ -value determination of 1.2 and 0.1 V cathodic current. (d) Capacitive-controlled charge storage contributions separated by cyclic voltammogram at  $5 \text{ mV s}^{-1}$  scan.

a Coulombic efficiency (CE) of 59.54% in the initial cycle. The initial irreversible loss is ascribed to the formation of the SEI layer. In addition, the reversible capacity of the  $\text{PMo}_{12}$ -PPy/RGO nanocomposite can reach  $1013 \text{ mAh g}^{-1}$  after 50 cycles, whereas the control samples only deliver discharge capacities of  $1507.3 \text{ mAh g}^{-1}$  and the remaining capacity is  $500.9 \text{ mAh g}^{-1}$  after 50 cycles ( $\text{PMo}_{12}$ /RGO) and discharge capacities of  $856.2 \text{ mAh g}^{-1}$  and the residual capacity is  $270.3 \text{ mAh g}^{-1}$  up to 50 cycles ( $\text{PMo}_{12}$ ). The above results demonstrate that the chemisorptions of  $\text{PMo}_{12}$  between the interfaces of PPy and RGO gives a superior electrode performance in LIBs compared with that of  $\text{PMo}_{12}$ /RGO and pure  $\text{PMo}_{12}$ . The capacity performance of the  $\text{PMo}_{12}$ -PPy/RGO nanocomposite is also superior to that of the  $\text{CoMo}_6$ -PPy/RGO nanocomposite and the  $(\text{NH}_4)_6\text{Mo}_7$ -PPy/RGO nanocomposite (Figure S7a). This cycling capacity is higher than most of the pristine POMs and POMs-based nanocomposite electrodes that ever reported (Table S1 in the Supporting Information).

Because the high rate capability is beneficial to the design of high-power-type LIBs anode materials, excellent rate performance of the electrode is also an important aspect for evaluating many practical application of LIBs. It can be found that the discharge capacity of  $\text{PMo}_{12}$ -PPy/RGO nanocomposite remains at 1057.5, 905.9, 688.0, 510.7, and  $316.4 \text{ mAh g}^{-1}$  at a rate of 0.1, 0.2, 0.5, 1, and  $2 \text{ A g}^{-1}$ , respectively. Moreover, when reducing the current back to  $0.1 \text{ A g}^{-1}$ , a high capacity of  $1030.2 \text{ mAh g}^{-1}$  is quickly resumed, suggesting a good reversibility of the  $\text{PMo}_{12}$ -PPy/RGO nanocomposite (Figure 2d). In contrast, the  $\text{CoMo}_6$ -PPy/RGO nanocomposite and the  $(\text{NH}_4)_6\text{Mo}_7$ -PPy/RGO nanocomposite electrodes show a faster capacity fading as the charge/discharge rates increase (Figure S7b). In addition, a long-term cycling is achievable for  $\text{PMo}_{12}$ -PPy/RGO, which maintained a capacity of  $372.24 \text{ mAh g}^{-1}$  after 400 cycles at  $2 \text{ A g}^{-1}$  (Figure S9). For proving the structural stability of  $\text{PMo}_{12}$ -PPy/RGO, we performed the SEM analysis after 50 cycles at  $500 \text{ mAh g}^{-1}$ . As shown in

Figure S10, the good structural integrity is well retained compared with the  $\text{CoMo}_6$ -PPy/RGO and the  $(\text{NH}_4)_6\text{Mo}_7$ -PPy/RGO, indicating the stability of the electrode.

On the basis of the excellent performance of  $\text{PMo}_{12}$ -PPy/RGO, effects of different concentrations of  $\text{PMo}_{12}$  on the electrocatalytic activity of  $\text{PMo}_{12}$ -PPy/RGO-3 and  $\text{PMo}_{12}$ -PPy/RGO-4 were investigated. As seen from Figure S8a, they showed a relatively poor capacity performance.  $\text{PMo}_{12}$ -PPy/RGO-1 and  $\text{PMo}_{12}$ -PPy/RGO-2 also exhibited poor capacity performance (Figure S8b), which can be attributed to the low concentration of GO loading with poor conductivity and low electron transfer efficiency. In contrast, a high-concentration loading may lead to the restacking of GO and affect the distribution of the mesopores for improving the accessibility of  $\text{Li}^+$  and electrons.

To profoundly explain the better performance of the  $\text{PMo}_{12}$ -PPy/RGO nanocomposite electrodes, we carried out an analysis of the electrochemical impedance spectroscopy (EIS) of  $\text{PMo}_{12}$ -PPy/RGO anode after three cycles (Figure 3a). The EIS data were analyzed via fitting to the equivalent circuit model (the detail inset in Figure 3a).<sup>40</sup> The  $R_1$  consists of the total resistance of the electrolyte, separator, and electrical contacts,  $R_2$  is the charge transfer resistance,  $W$  is the Warburg impedance, and constant phase element of the electrode/electrolyte interface (CPE) is associated with the interfacial resistance. It can be observed that the charge transfer resistance of  $\text{PMo}_{12}$ -PPy/RGO is  $90.25 \Omega$ , which is much lower than that of  $\text{PMo}_{12}$  ( $645 \Omega$ ). These results confirm that the incorporation of PPy coating and RGO can be favorable to charge transfer and improve the  $\text{Li}^+$  kinetics during the charge/discharge processes.

The reversible capacity of  $\text{PMo}_{12}$ -PPy/RGO is about  $1082.5 \text{ mAh g}^{-1}$  at  $100 \text{ mA g}^{-1}$ , whereas the theoretical capacity of  $\text{PMo}_{12}$ -PPy/RGO was calculated to be about  $835 \text{ mAh g}^{-1}$  (details can be seen in Supporting Information). Herein, we speculate this value exceeds the theoretical one on the account

of a hybrid battery–supercapacitor consisting of POMs, RGO, and PPy. The battery component is caused by the reversible redox reactions of metal ions (Mo) during the lithiation/delithiation cycles. At the same time, the capacitive behavior also promotes the performances, which is ascribed to RGO and PPy.<sup>41</sup> To investigate the electrochemical behavior of PMo<sub>12</sub>–PPy/RGO, the CV profiles at different scan rates (0.2–10 mV s<sup>−1</sup>) were performed between 0.01 and 3.0 V (Figure 3b). The voltammetric response of the PMo<sub>12</sub>–PPy/RGO electrode was analyzed by the power law  $I = a \times v^b$ , where  $I$  represents the current,  $v$  is the scan rate, and  $a$  is an alterable parameter. When  $b = 0.5$ , the electrode reaction is regarded as a behavior that is controlled by the diffusion of Li<sup>+</sup>,<sup>41–44</sup> whereas  $b = 1$  indicates a surface-controlled charge storage process. As shown in Figure 3c, it is worth noting that the  $b$  value at 0.1 V was determined to be about 0.6349, whereas the  $b$  value at 1 V was about 0.6796, suggesting a hybrid of both. To further understand the energy storage mechanism of PMo<sub>12</sub>–PPy/RGO, the equations as discussed below are utilized to calculate the contributions of the capacitance and intercalation capacity.

$$i(v) = k_1v + k_2v^{0.5}$$

or

$$i(v)/v^{0.5} = k_1v^{0.5} + k_2$$

where  $k_1v$  and  $k_2v^{0.5}$  correspond to the current contributions “ $i$ ” arising from the surface capacitive effect and the diffusion-controlled process, respectively, at a give potential “ $v$ .”<sup>45–47</sup> Figure 3d shows that the capacitive-controlled capacity contributed about 27.1% of the total Li<sup>+</sup> storage for PMo<sub>12</sub>–PPy/RGO at 5 mV s<sup>−1</sup> (the blue-shaded area of Figure 3d).

The superior electrode performance can be ascribed to the structure and composition of the PMo<sub>12</sub>–PPy/RGO nanocomposite. First, the RGO films are employed here for their intrinsically excellent conductivity; they can also be used as excellent supports. The PMo<sub>12</sub>–PPy nanoparticles can be distributed homogeneously on the flaky RGO films, which hampers restacking among the layers, thus relieving the structure destruction taking place in the electrodes during cycling.<sup>48</sup> Second, the PMo<sub>12</sub>–PPy/RGO nanocomposite shows a hybrid behavior of battery and supercapacitor. The battery behaviors of PMo<sub>12</sub> are achieved by the redox of metal ions (Mo). At the same time, the capacitive behavior also promotes the performance, which is ascribed to RGO and PPy. Third, the porous structure of the PMo<sub>12</sub>–PPy/RGO nanocomposite offers a lot of active sites for Li<sup>+</sup> storage, as well as sufficient contact between the PMo<sub>12</sub>–PPy/RGO electrode and electrolyte. Accordingly, the specific capacity and rate capability of PMo<sub>12</sub>–PPy/RGO are enhanced.

### 3. CONCLUSIONS

In conclusion, we synthesized the PMo<sub>12</sub>–PPy/RGO nanocomposite through a simple one-pot hydrothermal method. The charge/discharge measurements of the PMo<sub>12</sub>–PPy/RGO nanocomposite represent the highest capacity and the most robust charge/discharge rate among the microcrystal PMo<sub>12</sub>, PMo<sub>12</sub>/RGO, CoMo<sub>6</sub>–PPy/RGO, and (NH<sub>4</sub>)<sub>6</sub>Mo<sub>7</sub>–PPy/RGO. Furthermore, the PMo<sub>12</sub>–PPy/RGO exhibits a high capacity over 1000 mAh g<sup>−1</sup>, a long-term cycling with more than 400 cycles at 2 A g<sup>−1</sup>, and a good rate performance. The results demonstrates that we have successfully immobilized POMs to RGO via the wrapping of PPy and the anode

materials also exhibits a hybrid behavior of a battery–supercapacitor for superior lithium storage, which inspires us to explore advanced and insoluble framework materials consisting of electroactive molecule or cluster units for Li- and Na-storage.

### 4. EXPERIMENTAL SECTION

**4.1. Reagents.** All of the chemicals were purchased and used without further purification. The water used in the experiments was ultrapurified water (18.25 MΩ). The natural graphite powder was purchased from Aladdin. Potassium permanganate (KMnO<sub>4</sub>, ≥99%), hydrogen peroxide (H<sub>2</sub>O<sub>2</sub>, 30%), hydrazine hydrate (HCl, 36%), concentrated sulfuric acid (H<sub>2</sub>SO<sub>4</sub>, 98%) hexaammonium molybdate ((NH<sub>4</sub>)<sub>6</sub>Mo<sub>7</sub>O<sub>24</sub>·4H<sub>2</sub>O), and phosphomolybdic acid (H<sub>3</sub>PMo<sub>12</sub>O<sub>40</sub>·*n*H<sub>2</sub>O) were purchased from Sinopharm Chemical Reagent Co., Ltd. Phosphorus pentoxide (P<sub>2</sub>O<sub>5</sub>, ≥98.0%), potassium persulfate (K<sub>2</sub>S<sub>2</sub>O<sub>8</sub>, ≥99.5%), and were purchased from Shanghai Lingfeng Chemical Reagent Co., Ltd. Pyrrole (C<sub>4</sub>H<sub>5</sub>N, ≥98.0%) was purchased from Shanghai Kefeng Industry & Commerce Co., Ltd.

GO was prepared by modified Hummer's method.<sup>49</sup> The POMs clusters (NH<sub>4</sub>)<sub>4</sub>[CoMo<sub>6</sub>O<sub>24</sub>]·7H<sub>2</sub>O (CoMo<sub>6</sub>) was synthesized according to the literature method.<sup>50</sup>

#### 4.2. Synthesis of the PMo<sub>12</sub>–RGO Nanocomposite.

GO is dispersed in deionized water (10 mL) and sonicated to form a suspension with a concentration of 2 mg mL<sup>−1</sup>, followed by the introduction of the solution of 109 μL Py in 1 mL of ethanol. Then, magnetic stirring was maintained for about 30 min. After that, PMo<sub>12</sub> (0.25 mmol, 0.456 g) was added into the PPy/GO mixture with continuous stirring. The mixture was transferred into a stainless steel vessel maintained at 180 °C for 12 h. The product was filtrated and washed with water and ethanol at least three times. After drying in vacuum oven at 60 °C for about 24 h, the resulting sample was obtained. On the basis of the experiment, we obtained the as-prepared composite PMo<sub>12</sub>–PPy/RGO (0.2991 g) and calculated the content of RGO to be about 6.67%. For comparison, CoMo<sub>6</sub>–PPy/RGO and (NH<sub>4</sub>)<sub>6</sub>Mo<sub>7</sub>–PPy/RGO were synthesized in similar method, except that PMo<sub>12</sub> was replaced by CoMo<sub>6</sub> and (NH<sub>4</sub>)<sub>6</sub>Mo<sub>7</sub> in the respective reactions, and PMo<sub>12</sub>/RGO was synthesized by identical experimental without adding Py. In control experiments, PMo<sub>12</sub>–PPy/RGO-1, PMo<sub>12</sub>–PPy/RGO-2, PMo<sub>12</sub>–PPy/RGO-3, and PMo<sub>12</sub>–PPy/RGO-4 were synthesized by the similar synthetic method. The samples defined as PMo<sub>12</sub>–PPy/RGO-1 and PMo<sub>12</sub>–PPy/RGO-2 were obtained by altering the GO loading, corresponding to 1 and 3 mg mL<sup>−1</sup>, respectively. The samples defined as PMo<sub>12</sub>–PPy/RGO-3 and PMo<sub>12</sub>–PPy/RGO-4 were obtained by altering the concentration of PMo<sub>12</sub>, corresponding to 20 and 30 mM, respectively.

**4.3. Material Characterization.** The FTIR was collected on a Nexus 670 spectrometer. The Raman measurements were carried out using a Renishaw inVia Raman Microscope (532 nm). The thermogravimetric analysis (TGA) was carried out by using a Shimadzu-60 thermoanalyzer in air argon with a heating rate of 10 °C min<sup>−1</sup> from room temperature to 1100 °C. Nitrogen adsorption–desorption isotherms were evaluated at 77 K on a Micromeritics ASAP 2050 system, whereas the pore size distributions were calculated according to the Barrett–Joyner–Halenda formula. The TEM and high-resolution TEM images were captured by JEOL-2100F apparatus and JEOL JSM-6700 M scanning electron microscope, respectively. The energy-dispersive X-ray (EDX) was performed on JSM-5160LV-Vantage typed energy spectrometer. The XPS

measurements was collected on a scanning X-ray microprobe (PHI 5000 Versa; ULAC-PHI, Inc.) using the excitation energy of 1486.6 eV (Al  $K\alpha$ ) and the C 1s line at 284.8 eV as energy reference.

**4.4. Electrochemical Characterization.** To prepare a working electrode, a mixture of  $\text{PMo}_{12}$ -PPy/RGO (or  $\text{PMo}_{12}$ ,  $\text{PMo}_{12}$ /RGO,  $\text{CoMo}_6$ -PPy/RGO,  $(\text{NH}_4)_6\text{Mo}_7$ -PPy/RGO), carbon black, and poly(vinylidene fluoride) with a weight ratio of 7:2:1 were coated on a piece of copper foil. The active materials loading for the electrode was around 1 mg. The half-coin cells were assembled in an argon-filled glovebox utilizing Li metal as the negative electrode, a solution of 1 M  $\text{LiPF}_6$  in ethylene carbonate, dimethyl carbonate (1:1 in volume) as the electrolyte, and a Celgard 2400 membrane as the separator. The galvanostatic charge/discharge measurement was conducted by a LAND CT2001A multichannel battery between 0.01 and 3.0 V. The EIS measurements and CV were conducted on CHI 660D (Shanghai, China) electrochemical workstation.

## ■ ASSOCIATED CONTENT

### ■ Supporting Information

The Supporting Information is available free of charge on the ACS Publications website at DOI: 10.1021/acsomega.7b00752.

Structure and morphology characterizations including Raman, FTIR, SEM, TEM, EDX,  $\text{N}_2$  adsorption-desorption isotherm, TGA, XPS for  $\text{PMo}_{12}$ -PPy/RGO and other control samples (Figures S1–S6 and S10); cycle-life performance and rate capability test for  $\text{PMo}_{12}$ -PPy/RGO and other control samples (Figures S7 and S8); comparison of  $\text{PMo}_{12}$ -PPy/RGO with other POMs-based anodes (Table S1) (PDF)

## ■ AUTHOR INFORMATION

### Corresponding Author

\*E-mail: yqlan@njnu.edu.cn.

### ORCID

Long-Zhang Dong: 0000-0002-9276-5101

Dong-Sheng Li: 0000-0003-1283-6334

Ya-Qian Lan: 0000-0002-2140-7980

### Author Contributions

<sup>†</sup>M.Z. and T.W. contributed equally to this work.

### Notes

The authors declare no competing financial interest.

## ■ ACKNOWLEDGMENTS

This work was financially supported by NSFC (Nos. 21622104, 21371099, and 21471080); the NSF of Jiangsu Province of China (Nos. BK20130043 and BK20141445); the Priority Academic Program Development of Jiangsu Higher Education Institutions; and the Foundation of Jiangsu Collaborative Innovation Center of Biomedical Functional Materials.

## ■ REFERENCES

- (1) Kang, K.; Meng, Y. S.; Bréger, J.; Grey, C. P.; Ceder, G. Electrodes with High Power and High Capacity for Rechargeable Lithium Batteries. *Science* **2006**, *311*, 977–980.
- (2) Ryu, K. S.; Kim, K. M.; Park, N.-G.; Park, Y. J.; Chang, S. H. Symmetric redox supercapacitor with conducting polyaniline electrodes. *J. Power Sources* **2002**, *103*, 305–309.
- (3) Lee, S. W.; Yabuuchi, N.; Gallant, B. M.; Chen, S.; Kim, B.-S.; Hammond, P. T.; Shao-Horn, Y. High-power lithium batteries from

functionalized carbon-nanotube electrodes. *Nat. Nanotechnol.* **2010**, *5*, 531–537.

(4) Zhang, X.; Shi, W.; Zhu, J.; Kharistal, D. J.; Zhao, W.; Lalia, B. S.; Hng, H. H.; Yan, Q. High-Power and High-Energy-Density Flexible Pseudocapacitor Electrodes Made from Porous  $\text{CuO}$  Nanobelts and Single-Walled Carbon Nanotubes. *ACS Nano* **2011**, *5*, 2013–2019.

(5) Song, Y.-F.; Tsunashima, R. Recent advances on polyoxometalate-based molecular and composite materials. *Chem. Soc. Rev.* **2012**, *41*, 7384–7402.

(6) Wang, H.; Hamanaka, S.; Nishimoto, Y.; Irle, S.; Yokoyama, T.; Yoshikawa, H.; Awaga, K. In operando X-ray absorption fine structure studies of polyoxometalate molecular cluster batteries: polyoxometalates as electron sponges. *J. Am. Chem. Soc.* **2012**, *134*, 4918–4924.

(7) Kawasaki, N.; Wang, H.; Nakanishi, R.; Hamanaka, S.; Kitaura, R.; Shinohara, H.; Yokoyama, T.; Yoshikawa, H.; Awaga, K. Nanohybridization of polyoxometalate clusters and single-wall carbon nanotubes: applications in molecular cluster batteries. *Angew. Chem., Int. Ed. Engl.* **2011**, *50*, 3471–3474.

(8) Nishimoto, Y.; Yokogawa, D.; Yoshikawa, H.; Awaga, K.; Irle, S. Super-Reduced Polyoxometalates: Excellent Molecular Cluster Battery Components and Semipermeable Molecular Capacitors. *J. Am. Chem. Soc.* **2014**, *136*, 9042–9052.

(9) Ji, Y.; Huang, L.; Hu, J.; Streb, C.; Song, Y.-F. Polyoxometalate-functionalized nanocarbon materials for energy conversion, energy storage and sensor systems. *Energy Environ. Sci.* **2015**, *8*, 776–789.

(10) Huang, L.; Hu, J.; Ji, Y.; Streb, C.; Song, Y.-F. Pyrene-Anderson-Modified CNTs as Anode Materials for Lithium-Ion Batteries. *Chem. – Eur. J.* **2015**, *21*, 18799–18804.

(11) Ji, Y.; Hu, J.; Huang, L.; Chen, W.; Streb, C.; Song, Y.-F. Covalent Attachment of Anderson-Type Polyoxometalates to Single-Walled Carbon Nanotubes Gives Enhanced Performance Electrodes for Lithium Ion Batteries. *Chem. – Eur. J.* **2015**, *21*, 6469–6474.

(12) Abouimrane, A.; Compton, O. C.; Amine, K.; Nguyen, S. T. Non-Annealed Graphene Paper as a Binder-Free Anode for Lithium-Ion Batteries. *J. Phys. Chem. C* **2010**, *114*, 12800–12804.

(13) Wang, C.; Li, D.; Too, C. O.; Wallace, G. G. Electrochemical Properties of Graphene Paper Electrodes Used in Lithium Batteries. *Chem. Mater.* **2009**, *21*, 2604–2606.

(14) Liang, M.; Zhi, L. Graphene-based electrode materials for rechargeable lithium batteries. *J. Mater. Chem.* **2009**, *19*, 5871–5878.

(15) Ding, S.; Luan, D.; Boey, F. Y. C.; Chen, J. S.; Lou, X. W.  $\text{SnO}_2$  nanosheets grown on graphene sheets with enhanced lithium storage properties. *Chem. Commun.* **2011**, *47*, 7155–7157.

(16) Stoller, M. D.; Park, S.; Zhu, Y.; An, J.; Ruoff, R. S. Graphene-Based Ultracapacitors. *Nano Lett.* **2008**, *8*, 3498–3502.

(17) Kim, K. H.; Oh, Y.; Islam, M. F. Mechanical and Thermal Management Characteristics of Ultrahigh Surface Area Single-Walled Carbon Nanotube Aerogels. *Adv. Funct. Mater.* **2013**, *23*, 377–383.

(18) Zhang, D.; Zhang, X.; Chen, Y.; Wang, C.; Ma, Y. An environment-friendly route to synthesize reduced graphene oxide as a supercapacitor electrode material. *Electrochim. Acta* **2012**, *69*, 364–370.

(19) Kume, K.; Kawasaki, N.; Wang, H.; Yamada, T.; Yoshikawa, H.; Awaga, K. Enhanced capacitor effects in polyoxometalate/graphene nanohybrid materials: a synergetic approach to high performance energy storage. *J. Mater. Chem. A* **2014**, *2*, 3801.

(20) Cui, Z.; Guo, C. X.; Yuan, W.; Li, C. M. In situ synthesized heteropoly acid/polyaniline/graphene nanocomposites to simultaneously boost both double layer- and pseudo-capacitance for supercapacitors. *Phys. Chem. Chem. Phys.* **2012**, *14*, 12823–12828.

(21) Jiang, M.; Zhu, D.; Zhang, H.; Zhao, X. Effective electron transfer between heteropoly blue and graphene oxide: a green approach to graphene synthesis. *New J. Chem.* **2014**, *38*, 3354–3357.

(22) Gómez-Romero, P.; Lira-Cantú, M. Hybrid organic–inorganic electrodes: The molecular material formed between polypyrrole and the phosphomolybdate anion. *Adv. Mater.* **1997**, *9*, 144–147.

(23) Li, H.; Pang, S.; Feng, X.; Mullen, K.; Bubeck, C. Polyoxometalate assisted photoreduction of graphene oxide and its nanocomposite formation. *Chem. Commun.* **2010**, *46*, 6243–6245.

- (24) Zhao, Y.; Liu, J.; Hu, Y.; Cheng, H.; Hu, C.; Jiang, C.; Jiang, L.; Cao, A.; Qu, L. Highly Compression-Tolerant Supercapacitor Based on Polypyrrole-mediated Graphene Foam Electrodes. *Adv. Mater.* **2013**, *25*, 591–595.
- (25) Wang, J.; Xu, Y.; Yan, F.; Zhu, J.; Wang, J. Template-free prepared micro/nanostructured polypyrrole with ultrafast charging/discharging rate and long cycle life. *J. Power Sources* **2011**, *196*, 2373–2379.
- (26) Zhang, X.; Zeng, X.; Yang, M.; Qi, Y. Investigation of a Branchlike MoO<sub>3</sub>/Polypyrrole Hybrid with Enhanced Electrochemical Performance Used as an Electrode in Supercapacitors. *ACS Appl. Mater. Interfaces* **2014**, *6*, 1125–1130.
- (27) Yang, Y.; Wang, C.; Yue, B.; Gambhir, S.; Too, C. O.; Wallace, G. G. Electrochemically Synthesized Polypyrrole/Graphene Composite Film for Lithium Batteries. *Adv. Energy Mater.* **2012**, *2*, 266–272.
- (28) Zhu, C.; Zhai, J.; Wen, D.; Dong, S. Graphene oxide/polypyrrole nanocomposites: one-step electrochemical doping, coating and synergistic effect for energy storage. *J. Mater. Chem.* **2012**, *22*, 6300–6306.
- (29) Zhou, D.; Han, B.-H. Graphene-Based Nanoporous Materials Assembled by Mediation of Polyoxometalate Nanoparticles. *Adv. Funct. Mater.* **2010**, *20*, 2717–2722.
- (30) Rocchiccioli-Deltcheff, C.; Fournier, M.; Franck, R.; Thouvenot, R. Vibrational investigations of polyoxometalates. 2. Evidence for anion–anion interactions in molybdenum(VI) and tungsten(VI) compounds related to the Keggin structure. *Inorg. Chem.* **1983**, *22*, 207–216.
- (31) Li, J.-S.; Wang, Y.; Liu, C.-H.; Li, S.-L.; Wang, Y.-G.; Dong, L.-Z.; Dai, Z.-H.; Li, Y.-F.; Lan, Y.-Q. Coupled molybdenum carbide and reduced graphene oxide electrocatalysts for efficient hydrogen evolution. *Nat. Commun.* **2016**, *7*, No. 11204.
- (32) Chen, Y.; Han, M.; Tang, Y.; Bao, J.; Li, S.; Lan, Y.; Dai, Z. Polypyrrole–polyoxometalate/reduced graphene oxide ternary nanohybrids for flexible, all-solid-state supercapacitors. *Chem. Commun.* **2015**, *51*, 12377–12380.
- (33) Liu, C.-H.; Tang, Y.-J.; Wang, X.-L.; Huang, W.; Li, S.-L.; Dong, L.-Z.; Lan, Y.-Q. Highly active Co–Mo–C/NRGO composite as an efficient oxygen electrode for water–oxygen redox cycle. *J. Mater. Chem. A* **2016**, *4*, 18100–18106.
- (34) Wang, X.-L.; Tang, Y.-J.; Huang, W.; Liu, C.-H.; Dong, L.-Z.; Li, S.-L.; Lan, Y.-Q. Efficient Electrocatalyst for the Hydrogen Evolution Reaction Derived from Polyoxotungstate/Polypyrrole/Graphene. *ChemSusChem* **2017**, *10*, 2402–2407.
- (35) Dolbecq, A.; Compain, J.-D.; Mialane, P.; Marrot, J.; Sécheresse, F.; Keita, B.; Holzle, L. R. B.; Miserque, F.; Nadjo, L. Hexa- and Dodecanuclear Polyoxomolybdate Cyclic Compounds: Application toward the Facile Synthesis of Nanoparticles and Film Electrodeposition. *Chem. – Eur. J.* **2009**, *15*, 733–741.
- (36) Zhu, Y.; Yuan, Z.; Cui, W.; Wu, Z.; Sun, Q.; Wang, S.; Kang, Z.; Sun, B. A cost-effective commercial soluble oxide cluster for highly efficient and stable organic solar cells. *J. Mater. Chem. A* **2014**, *2*, 1436–1442.
- (37) Xia, F.; Hu, X.; Sun, Y.; Luo, W.; Huang, Y. Layer-by-layer assembled MoO<sub>2</sub>–graphene thin film as a high-capacity and binder-free anode for lithium-ion batteries. *Nanoscale* **2012**, *4*, 4707–4711.
- (38) Reddy, M. V.; Rao, G. V. S.; Chowdari, B. V. R. Metal Oxides and Oxysalts as Anode Materials for Li Ion Batteries. *Chem. Rev.* **2013**, *113*, 5364–5457.
- (39) Zhou, F.; Xin, S.; Liang, H.-W.; Song, L.-T.; Yu, S.-H. Carbon Nanofibers Decorated with Molybdenum Disulfide Nanosheets: Synergistic Lithium Storage and Enhanced Electrochemical Performance. *Angew. Chem., Int. Ed.* **2014**, *53*, 11552–11556.
- (40) Cui, L.; Shen, J.; Cheng, F.; Tao, Z.; Chen, J. SnO<sub>2</sub> nanoparticles@polypyrrole nanowires composite as anode materials for rechargeable lithium-ion batteries. *J. Power Sources* **2011**, *196*, 2195–2201.
- (41) Wang, J.; Tang, H.; Zhang, L.; Ren, H.; Yu, R.; Jin, Q.; Qi, J.; Mao, D.; Yang, M.; Wang, Y.; Liu, P.; Zhang, Y.; Wen, Y.; Gu, L.; Ma, G.; Su, Z.; Tang, Z.; Zhao, H.; Wang, D. Corrigendum: Multi-shelled metal oxides prepared via an anion-adsorption mechanism for lithium-ion batteries. *Nat. Energy* **2016**, *1*, No. 16072.
- (42) Yuan, T.; Jiang, Y.; Sun, W.; Xiang, B.; Li, Y.; Yan, M.; Xu, B.; Dou, S. Ever-Increasing Pseudocapacitance in RGO–MnO–RGO Sandwich Nanostructures for Ultrahigh-Rate Lithium Storage. *Adv. Funct. Mater.* **2016**, *26*, 2198–2206.
- (43) Simon, P.; Gogotsi, Y.; Dunn, B. Where Do Batteries End and Supercapacitors Begin? *Science* **2014**, *343*, 1210–1211.
- (44) Augustyn, V.; Simon, P.; Dunn, B. Pseudocapacitive oxide materials for high-rate electrochemical energy storage. *Energy Environ. Sci.* **2014**, *7*, 1597–1614.
- (45) Wei, T.; Zhang, M.; Wu, P.; Tang, Y.-J.; Li, S.-L.; Shen, F.-C.; Wang, X.-L.; Zhou, X.-P.; Lan, Y.-Q. POM-based metal-organic framework/reduced graphene oxide nanocomposites with hybrid behavior of battery-supercapacitor for superior lithium storage. *Nano Energy* **2017**, *34*, 205–214.
- (46) Wang, J.; Polleux, J.; Lim, J.; Dunn, B. Pseudocapacitive Contributions to Electrochemical Energy Storage in TiO<sub>2</sub> (Anatase) Nanoparticles. *J. Phys. Chem. C* **2007**, *111*, 14925–14931.
- (47) Brezesinski, T.; Wang, J.; Tolbert, S. H.; Dunn, B. Ordered mesoporous [alpha]-MoO<sub>3</sub> with iso-oriented nanocrystalline walls for thin-film pseudocapacitors. *Nat. Mater.* **2010**, *9*, 146–151.
- (48) Huang, X.; Zeng, Z.; Fan, Z.; Liu, J.; Zhang, H. Graphene-Based Electrodes. *Adv. Mater.* **2012**, *24*, 5979–6004.
- (49) Wang, H.; Cui, L.-F.; Yang, Y.; Casalongue, H. S.; Robinson, J. T.; Liang, Y.; Cui, Y.; Dai, H. Mn<sub>3</sub>O<sub>4</sub>–Graphene Hybrid as a High-Capacity Anode Material for Lithium Ion Batteries. *J. Am. Chem. Soc.* **2010**, *132*, 13978–13980.
- (50) Nomiya, K.; Takahashi, T.; Shirai, T.; Miwa, M. Anderson-type heteropolyanions of molybdenum(VI) and tungsten(VI). *Polyhedron* **1987**, *6*, 213–218.